remote sensing

MDPI

Article

Neural Network-Based Estimation of Near-Surface Air Temperature in All-Weather Conditions Using FY-4A AGRI Data over China

Hai-Lei Liu [1,*], Min-Zheng Duan [2,3], Xiao-Qing Zhou [1], Sheng-Lan Zhang [1], Xiao-Bo Deng [1] and Mao-Lin Zhang [1]

[1] College of Meteorological Observations, Chengdu University of Information Technology, Chengdu 610225, China; 3220308035@stu.cuit.edu.cn (X.-Q.Z.); zslan@cuit.edu.cn (S.-L.Z.); dxb@cuit.edu.cn (X.-B.D.); 3230308039@stu.cuit.edu.cn (M.-L.Z.)
[2] Institute of Atmospheric Physics, Chinese Academy of Sciences, Beijing 100029, China; dmz@mailiap.ac.cn
[3] College of Earth and Planetary Sciences, University of Chinese Academy of Sciences, Beijing 100049, China
* Correspondence: liuhailei@cuit.edu.cn

Abstract: Near-surface air temperature (T_a) estimation by geostationary meteorological satellites is mainly carried out under clear-sky conditions. In this study, we propose an all-weather T_a estimation method utilizing FY-4A Advanced Geostationary Radiation Imager (AGRI) and the Global Forecast System (GFS), along with additional auxiliary data. The method includes two neural-network-based T_a estimation models for clear and cloudy skies, respectively. For clear skies, AGRI LST was utilized to estimate the T_a ($T_{a,clear}$), whereas cloud top temperature and cloud top height were employed to estimate the T_a for cloudy skies ($T_{a,cloudy}$). The estimated T_a was validated using the 2020 data from 1211 stations in China, and the RMSE values of the $T_{a,clear}$ and $T_{a,cloudy}$ were 1.80 °C and 1.72 °C, while the correlation coefficients were 0.99 and 0.986, respectively. The performance of the all-weather T_a estimation model showed clear temporal and spatial variation characteristics, with higher accuracy in summer (RMSE = 1.53 °C) and lower accuracy in winter (RMSE = 1.88 °C). The accuracy in southeastern China was substantially better than in western and northern China. In addition, the dependence of the accuracy of the T_a estimation model for LST, CTT, CTH, elevation, and air temperature were analyzed. The global sensitivity analysis shows that AGRI and GFS data are the most important factors for accurate T_a estimation. The AGRI-estimated T_a showed higher accuracy compared to the ERA5-Land data. The proposed models demonstrated potential for T_a estimation under all-weather conditions and are adaptable to other geostationary satellites.

Keywords: all-weather; air temperature; AGRI; GFS; neural network

Citation: Liu, H.-L.; Duan, M.-Z.; Zhou, X.-Q.; Zhang, S.-L.; Deng, X.-B.; Zhang, M.-L. Neural Network-Based Estimation of Near-Surface Air Temperature in All-Weather Conditions Using FY-4A AGRI Data over China. *Remote Sens.* **2024**, *16*, 3612. https://doi.org/10.3390/rs16193612

Academic Editor: Gad Levy

Received: 16 August 2024
Revised: 24 September 2024
Accepted: 25 September 2024
Published: 27 September 2024

1. Introduction

Near-surface air temperature (T_a) is a key parameter for characterizing the near-surface atmospheric environment [1,2]. It is one of the basic types of observation data at meteorological stations. T_a has been widely used in hydrology, ecology, climatology, epidemiology, environmental science, and residential energy consumption [3–5]. Moreover, it serves as a key variable in land surface processes and climate models [6,7]. T_a with high spatiotemporal resolution is of great significance for better understanding and modeling complex surface processes [8].

Generally, the T_a varies greatly in time and space [9,10]. A variety of factors, such as radiation, elevation, latitude, cloud cover, land surface type, and soil moisture, can influence T_a [11]. At present, the T_a is mainly obtained by routine observation at meteorological stations. Station observations can provide high temporal resolution and accurate T_a, but it only represents discrete point data [12]. In general, the distribution of sites is usually spatially heterogeneous due to the influence of the economy, population, and topography [13]. For example, the stations in southeastern China are dense, while those

in western China are sparse. About 90% of the national-level automatic weather stations managed by the China Meteorological Administration are located in eastern China, with low elevation (i.e., <2000 m), while there are few stations in areas above 5000 m [14,15].

Although two-dimensional T_a values can be obtained by interpolating station data, the accuracy of this method is typically influenced by meteorological station density, landscape, and terrains and conditions [16,17]. As a result, it is difficult to obtain high-precision T_a spatial distribution by interpolation, especially in complex terrain areas with few stations. Reanalysis and numerical weather prediction models can provide seamless global T_a data [13,18]. This is crucial for regions lacking meteorological stations [19]. These data typically have coarse spatial (e.g., 0.25°–0.5°) and temporal resolutions (e.g., 3 h) [14]. Coarse spatial resolution makes it difficult to provide fine T_a spatial variation and may bring larger uncertainty to applications at local scales [20]. Although NWP models cannot provide fine T_a data, they can significantly enhance T_a estimation accuracy integrated with satellite data [21].

Satellite-derived land surface temperature (LST) is extensively utilized for estimating T_a because of its high correlation with the T_a [16,22]. Currently, T_a estimation methods based on meteorological satellite data can be classified into statistical methods, temperature–vegetation index (TVX) methods, and energy balance methods [23]. Statistical methods typically incorporate multiple predictors, including LST and elevation in the T_a estimation model, employing multiple linear regression or nonlinear models to estimate T_a [24–26].

Machine learning models such as neural network (NN) and random forests can better express the complex relationships between predictors and T_a. Therefore, they usually have higher accuracy [27]. The TVX method is unsuitable for regions with sparse vegetation or bare land [22,28,29]. As a physical method, the energy balance method demands numerous inputs, many of which are typically not directly obtainable via satellite data [30,31].

Zhang et al. [32] utilized LST data from the FY-4A satellite to estimate hourly surface air temperature under clear-sky conditions. In short, the current T_a estimation methods typically rely on LST and supplementary parameters. Infrared radiation cannot penetrate clouds due to its short wavelength [33]. Therefore, LST is only available from infrared observations under clear sky, and the previous methods were mainly restricted to T_a estimation for clear-sky conditions ($T_{a,clear}$). However, more than 60% of the Earth's surface is covered by clouds [34]. This makes T_a estimation under cloudy skies ($T_{a,cloudy}$) an urgent issue to address. Liu et al. [35] employed geostationary meteorological satellite data to propose a high-spatial-resolution (i.e., 250 m) all-weather near-surface air temperature estimation method. However, their study was limited to the Hunan Province, and is yet to be broadly validated in other regions. Li et al. introduced an approach for $T_{a,cloudy}$ estimation using cloud top height and temperature (CTH and CTT) data from the Visible Infrared Imaging Radiometer (VIIRS) onboard NPP [36]. This approach is primarily derived from the atmospheric lapse rate (ALR) principle, and the RMSE of the estimated $T_{a,cloudy}$ was ~1.95 °C. This provides a possible approach for $T_{a,cloudy}$ estimation using satellite-derived cloud products.

It is important to make spatially continuous all-weather T_a with a high temporal resolution. Fengyun-4A (FY-4A) can continuously observe China and its surrounding regions with enhanced temporal and spatial resolution [22,37,38]. Since 1 August 2019, FY-4A LST, CTT, and CTH products have been available, which enhance the potential for all-weather T_a estimation at high temporal and spatial resolutions.

This research aims to establish a method for all-weather instantaneous T_a estimation using FY-4A and other auxiliary data over China. As far as we know, this is the first attempt to conduct all-weather T_a estimation utilizing geostationary satellite products. The structure of this paper is organized as follows: Section 2 outlines the datasets and the modeling approach used for all-weather T_a estimation. The data matching and prediction factor selection for T_a estimation are also shown in this section. Section 3 details the results and provides an error analysis of AGRI-derived T_a under both clear and cloudy conditions.

The comparisons with ERA5-Land and how model accuracy depends on various prediction factors are also addressed. Finally, the conclusions are summarized.

2. Materials and Methods

2.1. Data

The data used primarily consisted of (1) T_a at meteorological stations; (2) AGRI Level-2 LST, CTT and CTH products; (3) GFS T_a forecast field; (4) ERA5-Land T_a data; and (5) additional auxiliary data, including elevation, longitude, latitude, NDVI, and time information (i.e., Julian day (JD) and hour).

2.1.1. Station Data

The hourly T_a of 2423 national-level automatic weather stations over China in 2020 were used. The dataset was downloaded through China Meteorological Data Service Centre (CMDC). The T_a datasets had undergone strict quality control measures such as regional boundary-value checks, climatological boundary-value checks, spatial and temporal consistency checks, achieving an availability of ~99.9% [39]. According to the installation specification document of CMA, the thermometers were installed in the shelter about 1.5 m above the ground. Thus, the station T_a used in this study represents air temperature at 1.5 m. The topography and geolocation of the stations used are presented in Figure 1. Stations in eastern China are relatively dense, while those in the west (e.g., Qinghai–Tibet Plateau) are relatively sparse.

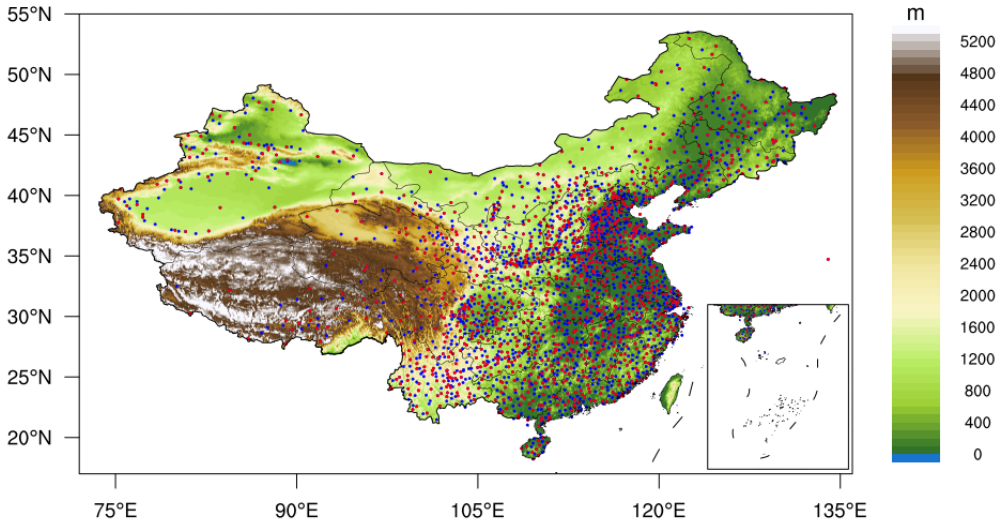

Figure 1. Geolocation of the stations used in this study over China. The sites of training and validation data for the near-surface air temperature (T_a) estimation model are marked in blue and red colors.

Table 1 presents the station numbers at various elevation intervals, with >75% of stations located at lower elevation (i.e., <1 km), ~20% of stations at 1–3 km, and only 86 stations (~3.55%) at >3 km. The purpose of this study is to estimate the T_a in the area without meteorological stations. We are inclined to think that half of the stations for modeling and other half of the stations for evaluation can better evaluate the applicability of the model. One half of the station data was used to build the models, while the other half was used to validate them.

Table 1. The distributions of the meteorological stations at different elevation intervals.

Elevation (km)	Sites Number	Percent (%)
<0.0	1	0.04
0.0–1.0	1831	75.57
1.0–2.0	427	17.62
2.0–3.0	78	3.22
3.0–4.0	63	2.60
4.0–5.0	23	0.95

2.1.2. FY-4A/AGRI Data

The Advanced Geostationary Radiation Imager (AGRI), a key instrument aboard the FY-4A satellite, demonstrates better performance than its predecessors [2]. It is equipped with 14 spectral channels covering a range from 0.55 to 13.8 μm. Compared to the imagers on the FY-2 series, AGRI offers a broader array of spectral channels, faster imaging capabilities, and improved spatial resolution [2].

AGRI can perform full-disk scans in 15 min and can cover China and its neighboring regions within 5 min. It is comparable with Himawari-8 and GOES-R imagers [40]. Currently, AGRI has LST, CTT, CTH, and cloud mask products available. The LST products from AGRI are retrieved using split-window channel observations. Dong evaluated the applicability of nine candidate split-window LST algorithms to AGRI data [41]. The Ulivieri-and-Cannizzaro method was selected as the AGRI operational LST retrieval algorithm, which was consistent with the LST algorithm of GOES-R [41,42].

CTT and CTH were derived using the measurements from AGRI 11.2, 12.4, and 13.3 μm, combined with numerical forecast data using an iterative optimal estimation calculation [43]. AGRI CTT and CTH were extracted for each cloud pixel, following a method with the GOES-R CTT and CTH algorithms [44]. The AGRI cloud mask product (CLM) has four flags, including clear, cloud, probably clear, and probably cloud. The T_a estimation were performed only for clear and cloudy pixels in this study (CLM = 0 and 3).

2.1.3. GFS Data

The operational GFS provides 0.25°, 0.5°, and 1° gridded T_a data at global scale. The forecast output is produced hourly for the first 120 h, and then three-hourly for hours 120 to 384 (days 5–16). It is updated every 6 h. However, GFS historical data were available only at 3 h intervals. Thus, this study utilized three-hourly GFS T_a forecasts at a 0.25° grid for the year 2020. These historical data were obtained from the National Center for Atmospheric Research (NCAR), which maintains a comprehensive archive of GFS forecasts. Real-time GFS T_a forecasts can be accessed from the NCEP Products Inventory.

2.1.4. ERA5-Land Data

To further analyze the performance of AGRI T_a model, ERA5-Land T_a were utilized for comparison. ERA5-Land represents a new generation of reanalysis data, offering enhenced spatiotemporal resolution and accuracy over its predecessors [45]. ERA5-Land provides hourly surface variables at a 0.1° grid spacing. This data set was produced by rerunning land component of ERA5 climate reanalysis. The ERA5-Land hourly 2 m T_a ($T_{a,\mathrm{ERA5}}$) from 2020 were used.

2.1.5. Auxiliary Data

Studies have demonstrated that auxiliary data can improve T_a estimation [4]. Table 2 shows the primary predictors used in this study. The three-arc-second Shuttle Radar Topography Mission elevation (i.e., SRTM3) was utilized.

Table 2. The main characteristics of the primary data.

Abbreviation	Units	Spatial Resolution	Temporal Resolution	Source
LST	K	4 km	15 min	NSMC
CTT	K	4 km	15 min	NSMC
CTH	m	4 km	15 min	NSMC
GFS T_a	K	0.25°	3 h	UCAR
elevation	m	3 arc-s	-	NASA
NDVI	-	250 m	16 days	NASA
Latitude	-	4 km	-	NSMC
T_a	°C	Site	1 h	CMDC

Latitude and time information were taken from AGRI geolocation data. The MODIS 16-day NDVI product (i.e., MOD13Q1) was also used. MOD13Q1 is a level-3 gridded NDVI measured at 250 m resolution every 16 days. The elevation and NDVI data were then spatially resampled for alignment with AGRI and GFS grid data. The main characteristics, such as the temporal and spational resolution and data sources, are detailed in Table 2.

2.2. Methods

2.2.1. $T_{a,clear}$ Estimation Model

Previous researchers developed an approach for estimating $T_{a,clear}$ using AGRI observations, GFS water vapor, relative humidity, and additionalauxiliary parameters [46]. Their findings indicated that GFS water vapor and humidity significantly enhanced the $T_{a,clear}$ estimation accuracy.

Given that GFS provides T_a forecast products, the GFS T_a forecast field ($T_{a,gfs}$) was directly used instead of PWV and RH in this study. To simplify, elevation, longitude, and latitude are denoted as *ELE*, *Lon*, and *Lat* respectively. Assuming that $T_{a,clear}$ can be predicted by these variables, $T_{a,clear}$ is formulated as follows:

$$T_{a,clear} = f\left(LST,\ T_{a,gfs}, ELE, NDVI, Lat, Lon, JD, Hour\right) \quad (1)$$

f () represents the non-linear function for the $T_{a,clear}$ estimation model.

2.2.2. $T_{a,cloudy}$ Estimation Model

AGRI can only provide LST under clear sky. Therefore, the T_a estimation approach using LST is not applicable for $T_{a,cloudy}$ estimation. Li et al. developed a approach for $T_{a,cloudy}$ estimation in China, utilizing VIIRS CTT and CTH combined with other predictors [36]. The method is derived from the atmospheric lapse rate (*ALR*) principle, according to which, in the troposphere, air temperature typically decreases with altitude [47]. The air temperature (T) at a specific height (H) is determined as follows:

$$T = T_{a,cloudy} + ALR \times \left(H - H_{sta}\right) \quad (2)$$

where $T_{a,cloudy}$ is station T_a under cloudy conditions, and H_{sta} is the station's elevation. If T and H are assumed as *CTT* and *CTH*, $T_{a,cloudy}$ is then derived as follows:

$$T_{a,cloudy} = CTT - ALR \times \left(CTH - H_{sta}\right) \quad (3)$$

Considering that the ALR is steeper in summer, the applicability to other seasons requires further evaluation. In our study, we established an NN model for $T_{a,cloudy}$ estimation using AGRI CTT and CTH products. Subsequently, the $T_{a,cloudy}$ can be estimated as shown below:

$$T_{a,cloudy} = f\left(CTT, CTH, T_{a,gfs}, ELE, Lat, Lon, NDVI, JD, Hour\right) \quad (4)$$

where f () represents the non-linear function for $T_{a,cloudy}$ estimation model. Unlike in Li et al.'s approach, this study used the AGRI cloud products rather than polar satellite [36]. Furthermore, datasets from more stations (i.e., 2423 stations over China) for a longer period (i.e., the entire year of 2020) were used. This is crucial for assessing the applicability of the T_a estimation method under cloudy conditions.

2.2.3. Data Processing

The spatial resolutions of GFS (0.25° × 0.25°) and AGRI (4 km × 4 km) were different, and the elevations in GFS grid and AGRI pixels were usually inconsistent. Thus, it was necessary to correct GFS T_a according to the elevation difference. Generally, we can perform T_a correction using the ALR. However, the ALR is easily influenced by season, latitude, elevation, and relative humidity [48,49]. For example, the ALR during summer is more significant than in winter, and temperature inversion may occur in winter [49]. There are obvious differences in ALR between eastern and western China due to the topographic characteristics [50]. Therefore, air temperature correction based on specific ALR (i.e., -0.67 °C/100 m) values may introduce large errors, especially for temperature inversion conditions in winter.

In this study, we did not use ALR to correct GFS T_a. Instead, the GFS and AGRI elevations, as well as GFS T_a, were used as inputs for the NN model. It was expected that the NN model would correct the T_a difference caused by the elevation difference through training processes. A nearest neighbor approach was utilized to match the predictor data with the station T_a dataset. Specifically, we identified the closest GFS grid and AGRI pixel to each station location and extracted the corresponding meteorological variables for model training and validation. Finally, 4,943,142 spatiotemporal matching datasets were obtained. These datasets were categorized into clear (2,033,012) and cloudy (2,910,130) sky datasets according to AGRI CLM. Data from half of the stations randomly selected were utilized for constructing T_a estimation model, and the remaining data were utilized for model validation.

2.2.4. Neural Network Model

The NN model has been extensively employed in geophysical parameter estimation [15]. The multilayer feedforward NN was employed to construct the $T_{a,clear}$ and $T_{a,cloudy}$ models. These models were individually trained and evaluated based on the collocated clear and cloudy sky datasets.

To develop an effective neural network model, we selected a two-layer network structure. Experimental analysis determined that a configuration of 128 neurons per layer achieved a good balance between model convergence and computational efficiency. Hyperparameters were tuned using cross-validation, leading to the selection of an optimal learning rate (i.e., 0.001), number of hidden layers, and neuron count. The Adam optimizer was employed to ensure fast and stable convergence during training. To prevent overfitting, we implemented cross-validation and other techniques to ensure the model's generalization ability across different data subsets.

Figure 2 illustrates the flowchart for all-weather T_a estimation approach. In the process of T_a estimation, AGRI pixels were divided into clear and cloudy sky based on the CLM products. The clear and cloudy sky match-ups were input into the $T_{a,clear}$ and $T_{a,cloudy}$ NN estimation models, respectively. Next, the AGRI-derived $T_{a,clear}$ and $T_{a,cloudy}$ were combined to produce the T_a for all-weather conditions.

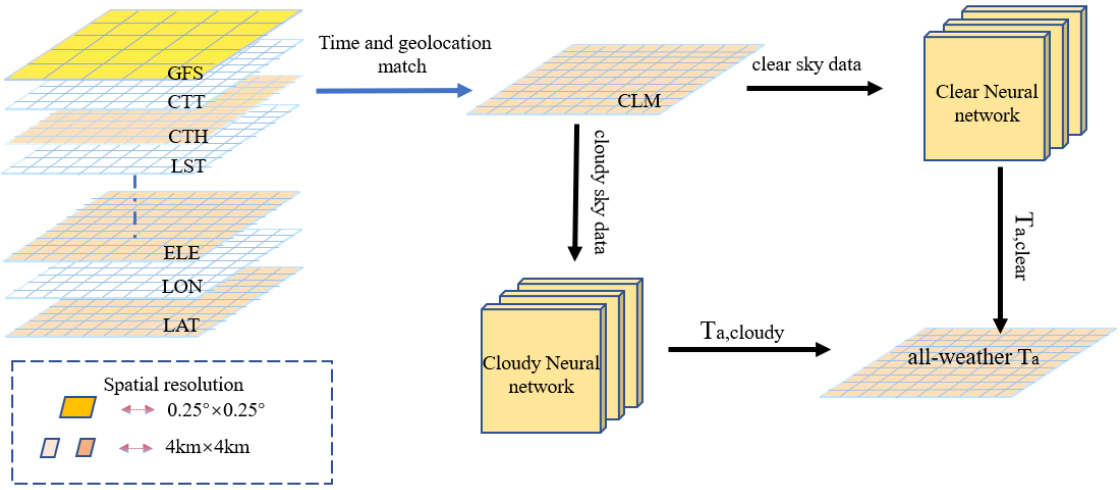

Figure 2. Flowchart of all-weather T_a estimation model incorporating multi-source data integration and neural networks.

2.2.5. Statistical Metrics

The correlation coefficient (R), root mean square error (RMSE), and bias were used to evaluate the T_a estimation models, as detailed below:

$$\mathrm{R} = \frac{\sum_{i=1}^{N}\left(T_a - \overline{T_a}\right)\left(T_{sta} - \overline{T_{sta}}\right)}{\sqrt{\sum_{i=1}^{N}\left(T_a - \overline{T_a}\right)^2 \sum_{i=1}^{N}\left(T_{sta} - \overline{T_{sta}}\right)^2}} \quad (5)$$

$$\mathrm{RMSE} = \sqrt{\frac{1}{N}\sum_{i=1}^{N}\left(T_a - T_{sta}\right)^2} \quad (6)$$

$$\mathrm{Bias} = \frac{1}{N}\sum_{i=1}^{N}\left(T_a - T_{sta}\right) \quad (7)$$

where T_a represents the estimated air temperature, T_{sta} is the in situ air temperature, and N is the overall count of samples.

3. Results

3.1. Overall Error Analysis

The AGRI T_a estimation model was assessed for clear and cloudy skies using station T_a, respectively. Figure 3 presents the 2D histograms comparing the estimated $T_{a,clear}$ and $T_{a,cloudy}$ with station data. Overall, the estimated $T_{a,clear}$ and $T_{a,cloudy}$ showed good agreement with station T_a. The performance of $T_{a,cloudy}$ was slightly better than that of $T_{a,clear}$. The correlation coefficients (R) for AGRI $T_{a,clear}$ and $T_{a,cloudy}$ were 0.990 and 0.986, with RMSE values of 1.78 °C and 1.67 °C, respectively. The biases for $T_{a,clear}$ and $T_{a,cloudy}$ were within ±0.03 °C, suggesting that the estimated T_a values for clear and cloudy sky were neither overestimated nor underestimated.

The estimated T_a of the two models became relatively discrete with in situ data when the T_a was lower than −20 °C. This means that the accuracy of the two models decreased slightly for low-T_a conditions, which might have been due to the fact that there were fewer samples at the boundary of the training data.

Figure 4 shows the T_a difference (AGRI T_a–in situ T_a) histograms for $T_{a,clear}$ and $T_{a,cloudy}$. The errors of both models showed a normal distribution, and most of the T_a differences were within ±2.5 °C (i.e., >80.95% samples). The samples with T_a differences of less than 2.0 °C accounted for 72.04% and 74.88% of the total for clear and cloudy sky, while those with less than 1.5 °C accounted for 60.65% and 64.01%, respectively. Satellite-derived T_{air} is typically regarded as 'accurate' when its accuracy range lies between 1 and 2 °C [51].

This indicates that the proposed models can accurately estimate $T_{a,clear}$ and $T_{a,cloudy}$ in most scenarios.

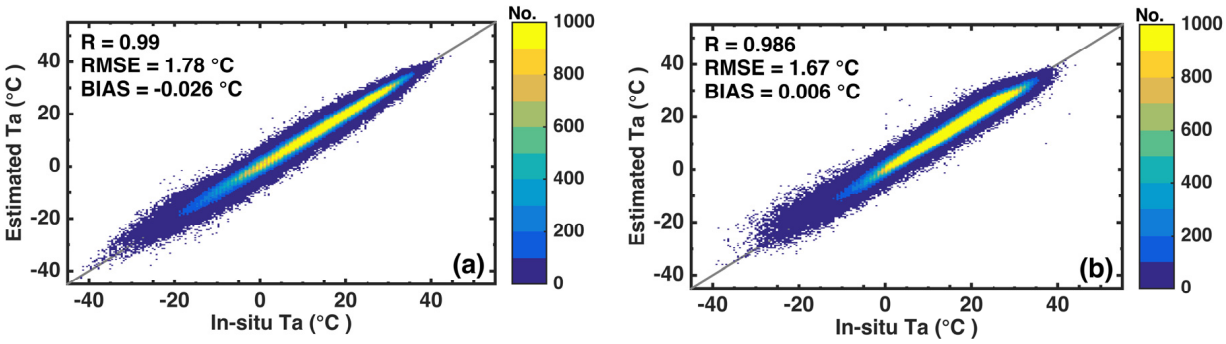

Figure 3. Two-dimensional histogram of AGRI-derived T_a under clear sky ($T_{a,clear}$) (**a**) and T_a under cloudy sky ($T_{a,cloudy}$) (**b**) versus in situ T_a at meteorological stations.

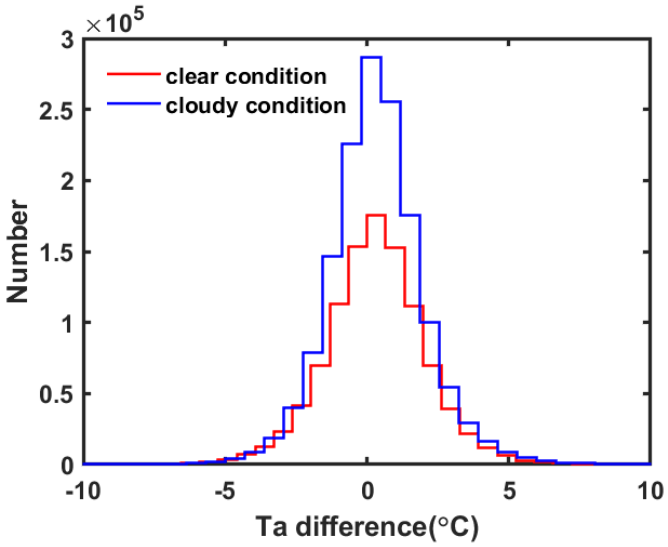

Figure 4. Histogram of T_a differences between the AGRI-estimated $T_{a,clear}$ (red) and $T_{a,cloudy}$ (blue) versus in situ T_a.

3.2. Spatial Distribution of Ta Error

The $T_{a,clear}$ and $T_{a,cloudy}$ estimation errors at each site were analyzed to comprehensively evaluate the T_a estimation models. Figure 5 depicts the spatial patterns of R, RMSE, and bias for $T_{a,clear}$ and $T_{a,cloudy}$. The $T_{a,clear}$ and $T_{a,cloudy}$ models both showed similar and clear spatial distribution patterns of errors. Both models performed better in eastern China than in western China, with lower RMSE and higher R values. The performance of the $T_{a,clear}$ model was comparable to that of the $T_{a,cloudy}$ model for most sites.

The correlation coefficient of the $T_{a,clear}$ and $T_{a,cloudy}$ models mainly varied from 0.97 to 0.99, while RMSE values spanning from 1.0 °C to 2.5 °C. The biases of the $T_{a,clear}$ and $T_{a,cloudy}$ models were mainly within ±1 °C for most sites. The RMSE values of the $T_{a,clear}$ and $T_{a,cloudy}$ model at ~45.22% and ~44.78% of the sites were less than 1.5 °C, while those at ~82.19% and ~83.58% of the sites were less than 2.0 °C, respectively. The RMSE values of the $T_{a,clear}$ and $T_{a,cloudy}$ models at most stations over southeast China were less than 1.7 °C, while those in northwest China were mainly 2.0–2.5 °C. These results could be attributed to several factors: (1) the influence of topography; (2) the density of the weather stations; and (3) the spatial distribution errors in the GFS T_a data.

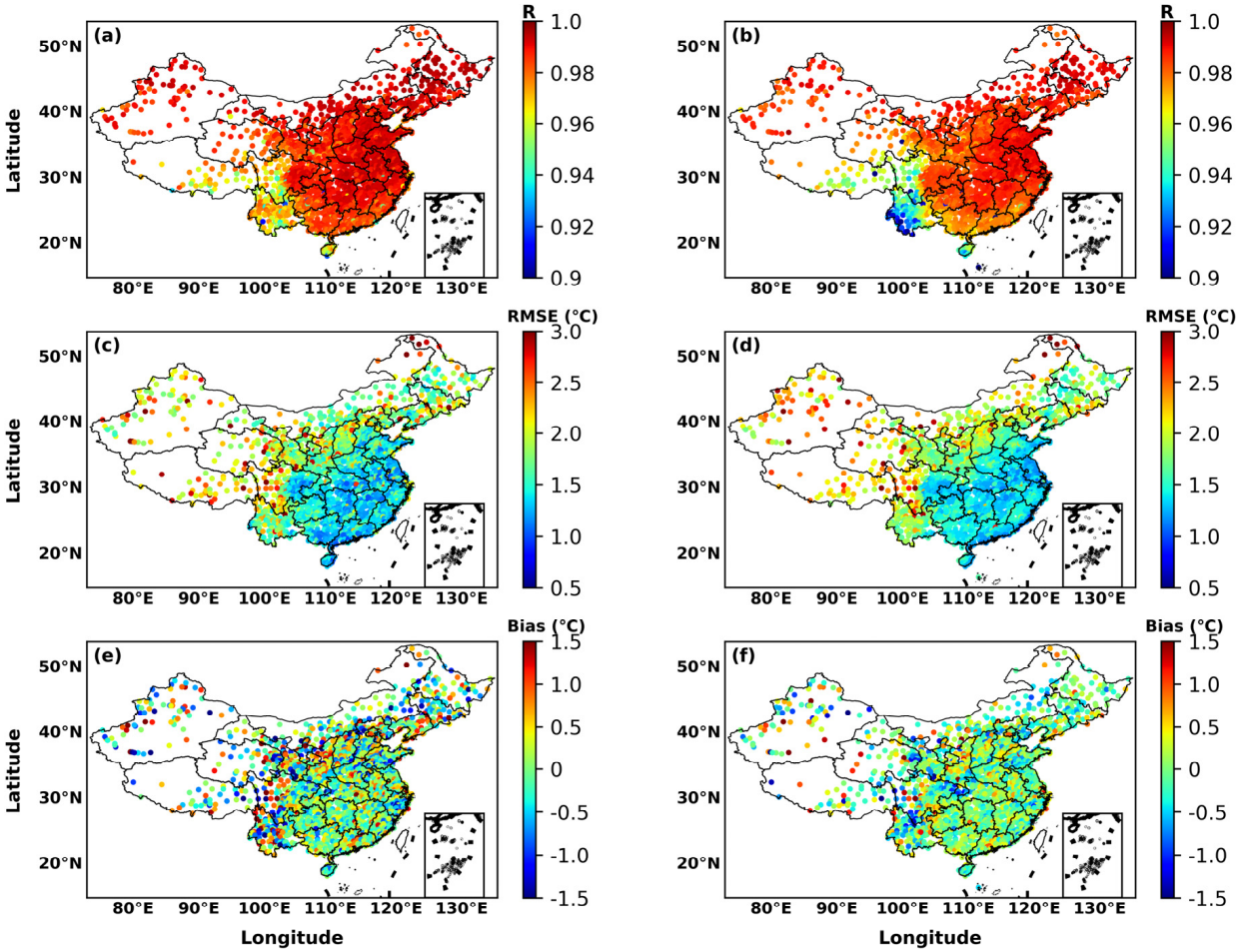

Figure 5. Spatial patterns of R (**a**,**b**), RMSE (**c**,**d**), and bias (**e**,**f**) for the AGRI-derived $T_{a,clear}$ (**left**) and $T_{a,cloudy}$ (**right**).

Compared to eastern China, western China features higher elevation and more intricate topography. This could lead to higher T_a heterogeneity, and a more complicated relationship between T_a and LST. Furthermore, the ALR in high-elevation and complex-topography areas is more complex than that in plain areas [49,50]. This makes it challenging to estimate the T_a using CTT and CTH in western China [36]. The weather stations in eastern China are dense, while those in western China are sparse. This makes the model constructed with data from all stations more applicable to eastern China. Previous studies have also shown that there is an obvious negative correlation between the RMSE of the estimated T_a and the number of stations [15,52]. Therefore, the low density of stations was another possible reason for the poor accuracy in western China.

As one of the key inputs for the T_a model, GFS T_a can significantly impact the model's performance. The GFS T_a error in western China was greater than that in eastern China. This might be a possible reason for the large error in the T_a estimation model in western region [21]. Additionally, factors such as variations in land cover types, vegetation effects, and differences in spatial scale between satellite and station measurements can also influence the spatial distribution of errors [53].

3.3. Seasonal Variation of T_a Estimation Error

Figure 6 shows the monthly RMSE variation of the $T_{a,clear}$ and $T_{a,cloudy}$, as well as the corresponding GFS T_a. The RMSE values for the AGRI and GFS $T_{a,clear}$ and $T_{a,cloudy}$ both exhibited distinct seasonal patterns. The RMSE was lowest during summer and peaked in winter. The maximum RMSE for the AGRI-estimated $T_{a,clear}$ was observed in January (~2.03 °C), after which it gradually declined, reaching a minimum value (~1.30 °C) in August. From September to December, the errors progressively increased.

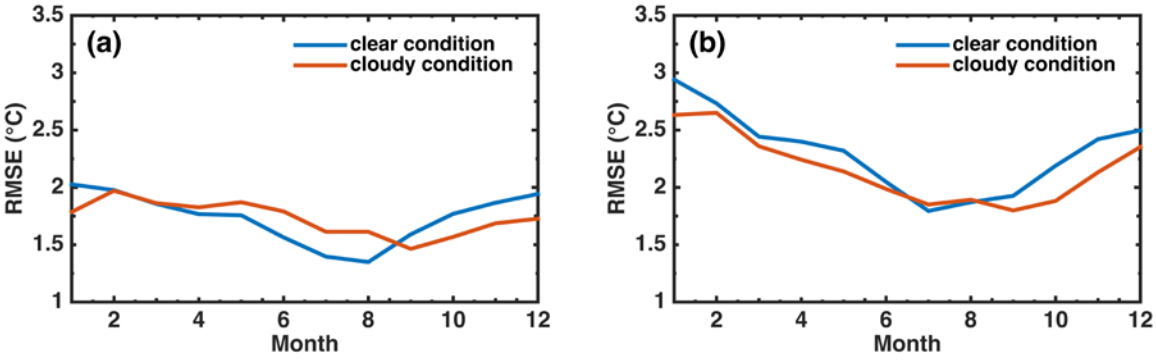

Figure 6. The monthly variation in RMSE for AGRI-derived (**a**) and GFS (**b**) $T_{a,clear}$ and $T_{a,cloudy}$.

The RMSE variation trend of the AGRI-estimated $T_{a,cloudy}$ was similar to that of the $T_{a,clear}$, but the highest RMSE of the $T_{a,cloudy}$ occurred in February (~1.98 °C), and the lowest in September (~1.42 °C). The RMSE of the AGRI-estimated $T_{a,clear}$ in summer was smaller than that of $T_{a,cloudy}$, while that of the AGRI $T_{a,clear}$ in winter was larger than that of $T_{a,cloudy}$.

The RMSE trends of the GFS $T_{a,clear}$ and $T_{a,cloudy}$ were similar to that of the AGRI-estimated T_a, but that of the AGRI T_a was 0.5–1.0 K smaller than that of the GFS. This indicates that GFS T_a has an important influence on the accuracy of the model. It is worth noting that the accuracy rates of the GFS $T_{a,clear}$ and $T_{a,cloudy}$ in July and August were comparable, and the accuracy of the GFS $T_{a,cloudy}$ in other months was better than that of the GFS $T_{a,clear}$. Comparatively, the AGRI $T_{a,clear}$ exhibited higher accuracy than $T_{a,cloudy}$ from April to August.

In general, the AGRI-estimated T_a demonstrated higher accuracy during summer compared to other seasons, which may have been due to the following reasons: (1) The dynamic variation range of summer T_a (e.g., diurnal variation) was smaller than in other seasons, which made the summer T_a estimation more reliable [54]. (2) The RMSE of the GFS T_a in summer was smaller than in other seasons. (3) The ALR was more obvious in summer, which improves the accuracy of summer $T_{a,cloudy}$ compared to other seasons.

The temporal variations of the AGRI-estimated all-weather T_a versus the instantaneous T_a measurements at 3 h intervals at four meteorological stations (randomly selected) in 2020 are shown in Figure 7. The station's latitude ranged from 25.6°N to 40.86°N, with the elevation ranging from 185.2 to 860.0 m. The T_a at these stations showed clear seasonal variation characteristics. The T_a values at these stations were higher during the summer and lower during the winter. The dynamic range of the T_a in summer was smaller than in other seasons. In general, the estimated T_a had a good agreement with the station data across different seasons for each site, with RMES values between 1.33 and 1.84 °C. The AGRI-estimated T_a could capture the seasonal and diurnal variation characteristics of air temperature. In addition, it was also shown that the $T_{a,clear}$ and $T_{a,cloudy}$ estimation models had good consistency.

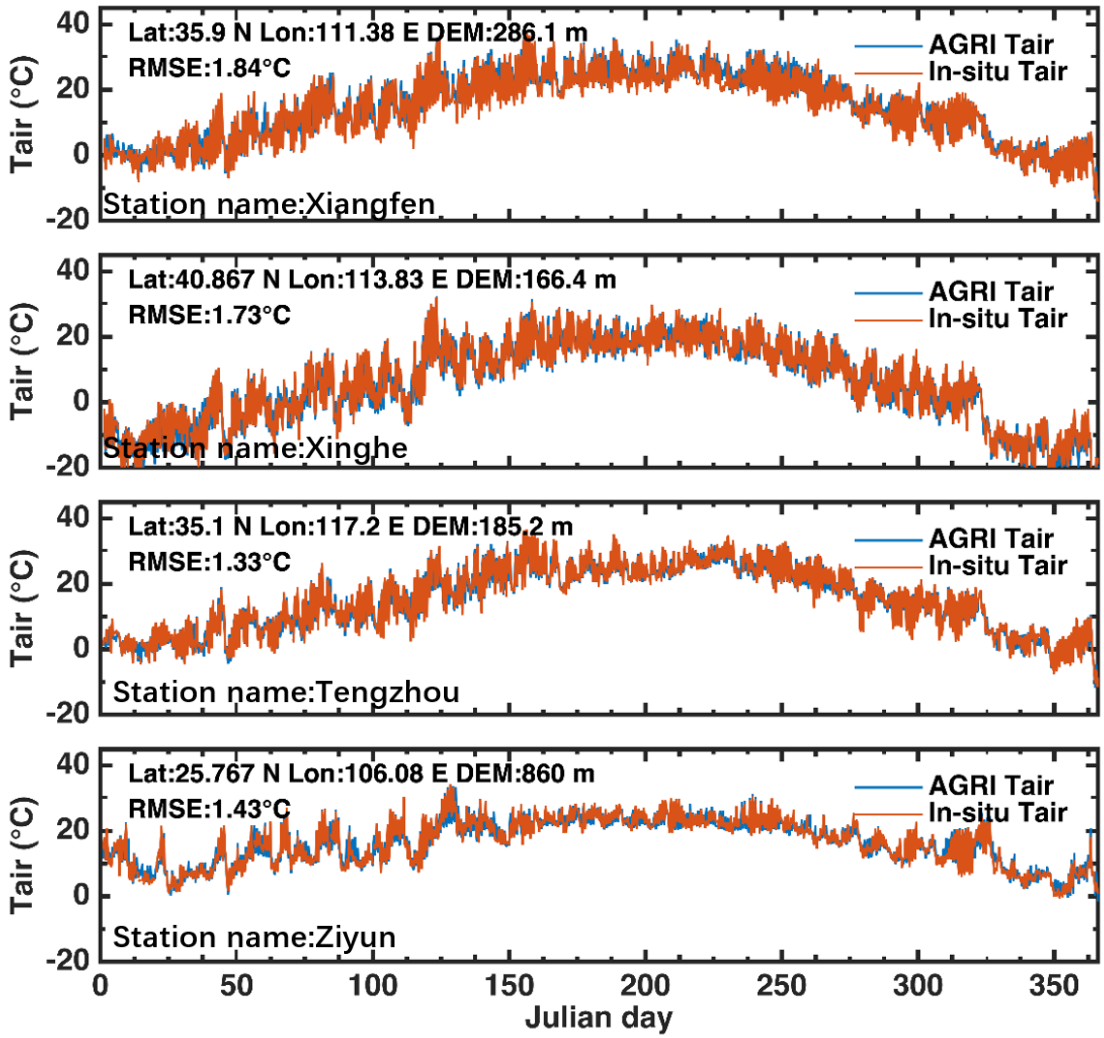

Figure 7. Time series of in situ and AGRI-derived all-weather T_a at 3 h intervals at four stations in 2020.

3.4. Comparisons with GFS/ERA5

Table 3 shows the validation results of the GFS, ERA5-Land, and AGRI T_a at different elevation intervals (i.e., 0–5.0 km with 1 km intervals). In general, the RMSE of the $T_{a,clear}$ and $T_{a,cloudy}$ of the three datasets increased with the elevation, and the accuracy rates of the GFS- and AGRI-estimated $T_{a,cloudy}$ were better than that of $T_{a,clear}$. This might have been due to the fact that the dynamic variation range of $T_{a,cloudy}$ is smaller than that of $T_{a,clear}$, which makes the prediction accuracy of T_a in cloudy sky better than in clear sky.

The AGRI-estimated T_a was consistently more accurate than GFS across all elevation intervals. The RMSE of the AGRI $T_{a,clear}$ was 0.75–1.15 °C lower than that of the GFS, while that of $T_{a,cloudy}$ was 0.22–0.56 °C lower than that of the GFS. This indicated that the contribution of AGRI data to the $T_{a,clear}$ model was greater than the contribution to the $T_{a,cloudy}$ model. This might be because the relationship between LST and T_a was stronger than that between cloud products and T_a. Furthermore, the RMSE difference between the GFS- and AGRI-estimated T_a showed a clear dependence on elevation, with the RMSE difference increasing with the elevation.

Table 3. Summary statistics of validation for GFS-, ERA5-Land-, and AGRI-estimated T_a for different elevation intervals with in situ observations for the period between 1 Jan 2020 and 31 Dec 2020.

Elevation (km)	Number	GFS			ERA5-Land			AGRI Ta		
		R	RMSE (°C)	Bias (°C)	R	RMSE (°C)	Bias (°C)	R	RMSE (°C)	Bias (°C)
Clear sky										
0.0–1.0	730,560	0.98	2.38	0.40	0.99	2.12	−0.29	0.99	1.62	−0.03
1.0–2.0	207,110	0.97	3.17	0.81	0.97	2.68	−0.01	0.99	2.02	−0.01
2.0–3.0	32,973	0.96	2.94	0.39	0.96	3.04	−0.57	0.98	2.17	0.17
3.0–4.0	33,997	0.94	3.42	0.18	0.92	4.36	−1.67	0.97	2.38	−0.12
4.0–5.0	11,866	0.94	3.43	0.37	0.95	3.55	−1.77	0.97	2.44	−0.06
All	1,016,506	0.98	2.62	0.47	0.98	2.39	−0.31	0.99	1.81	−0.02
Cloudy sky										
0.0–1.0	1,131,100	0.98	1.88	0.14	0.99	1.86	−0.21	0.99	1.54	0.01
1.0–2.0	237,650	0.97	2.41	0.36	0.98	2.38	−0.37	0.98	1.97	0.04
2.0–3.0	39,787	0.97	2.22	−0.09	0.95	3.49	−0.82	0.97	2.01	0.11
3.0–4.0	35,615	0.95	2.84	−0.54	0.92	4.47	−2.79	0.97	2.28	−0.17
4.0–5.0	10,913	0.95	3.09	−0.22	0.95	3.71	−2.08	0.96	2.62	0.24
All	1,455,065	0.98	2.01	0.15	0.98	2.15	−0.32	0.98	1.72	0.01

The performance of the AGRI-estimated T_a was also superior to that of the ERA5-Land T_a. The RMSE of the AGRI $T_{a,clear}$ was 0.50–1.98 °C smaller than that of the ERA5-Land T_a, while that of $T_{a,cloudy}$ was 0.34–2.19 °C smaller than that of the ERA5-Land. In a manner similar to the GFS data, the RMSE difference between the ERA5-Land- and AGRI-estimated T_a also increased with elevation. In addition, the accuracy values of the ERA5-Land $T_{a,clear}$ and $T_{a,cloudy}$ were slightly better than those of the GFS when the elevation was <2 km, and worse than those of the GFS when the elevation was >2 km. This showed that GFS can provide effective T_a information, and it was appropriate to take GFS T_a as one of the inputs for the model. The constraints of the AGRI and GFS data made the T_a estimation more accurate and reliable.

Figure 8 illustrates the spatial distribution of the all-weather T_a estimated by GFS, ERA5-Land, and AGRI at 12:00 UTC on 15 January, April, July, and October 2020. The T_a in China exhibited clear seasonal variation, characterized by higher T_a during summer and lower T_a during winter. In general, three datasets at four times showed similar T_a gradient distributions in most regions. It was clear that latitude and elevation have important influence on T_a distribution, with T_a decreases with the latitude and elevation. The T_a in southeast China at low-elevation areas was usually higher than in other areas (e.g., western China) for different seasons. The surface types also had an important impact on the T_a distribution. For example, the elevation of the Taklimakan desert (i.e., 36.5–41.2°N, 76.8–89.9°E) can reach up to 0.8–1.5 km. This region exhibited higher T_a values than other regions at the same elevation or latitude due to its surface type.

Overall, the datasets demonstrated consistent T_a distribution trends across various regions. However, there were also obvious T_a differences in some regions, such as the Tibetan Plateau, at 00 UTC on 15 January 2020. Specifically, the AGRI-estimated T_a was higher than those of the GFS and ERA5-Land over the Tibetan Plateau. The ERA5-Land and AGRI T_a at four times (Figure 9) were also individually validated with station data.

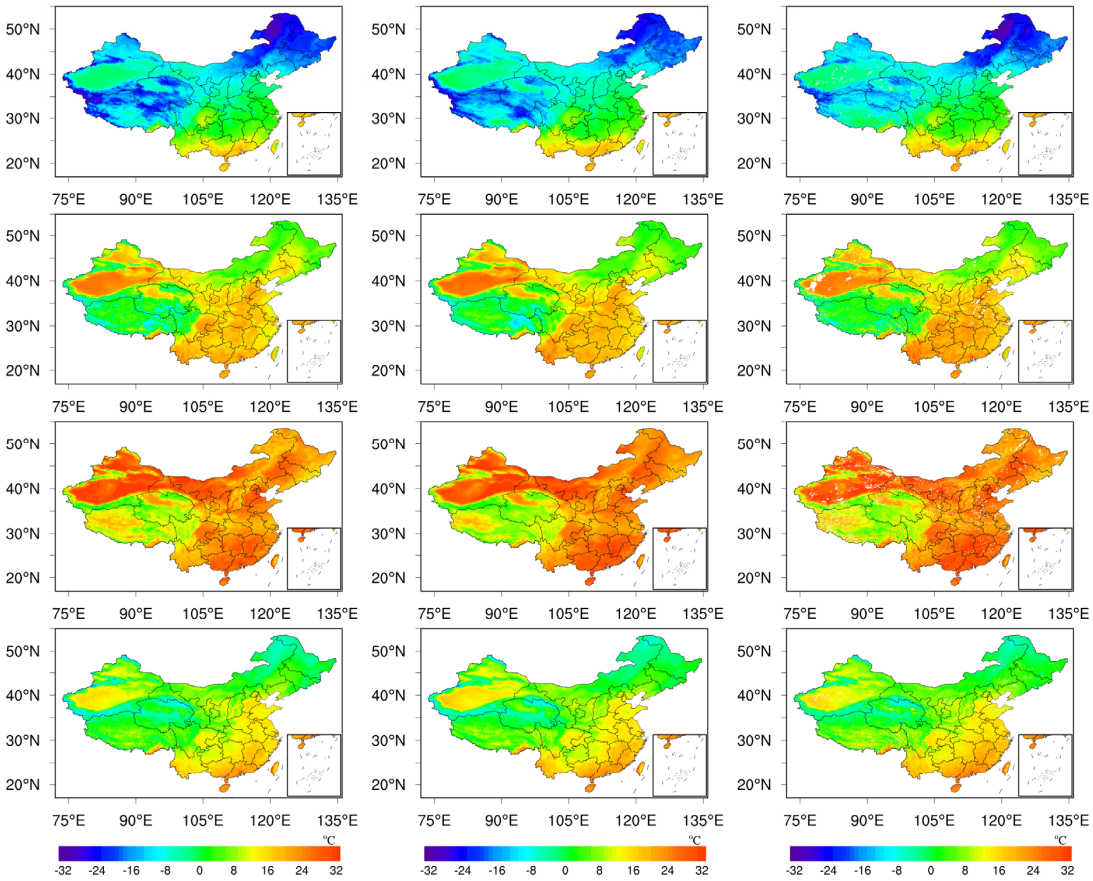

Figure 8. Comparison of the spatial pattern of GFS (first column), the ERA5−Land (second column) and AGRI-estimated all−weather T_a (third column) at 12:00 UTC on 15 January, April, July, and October 2020.

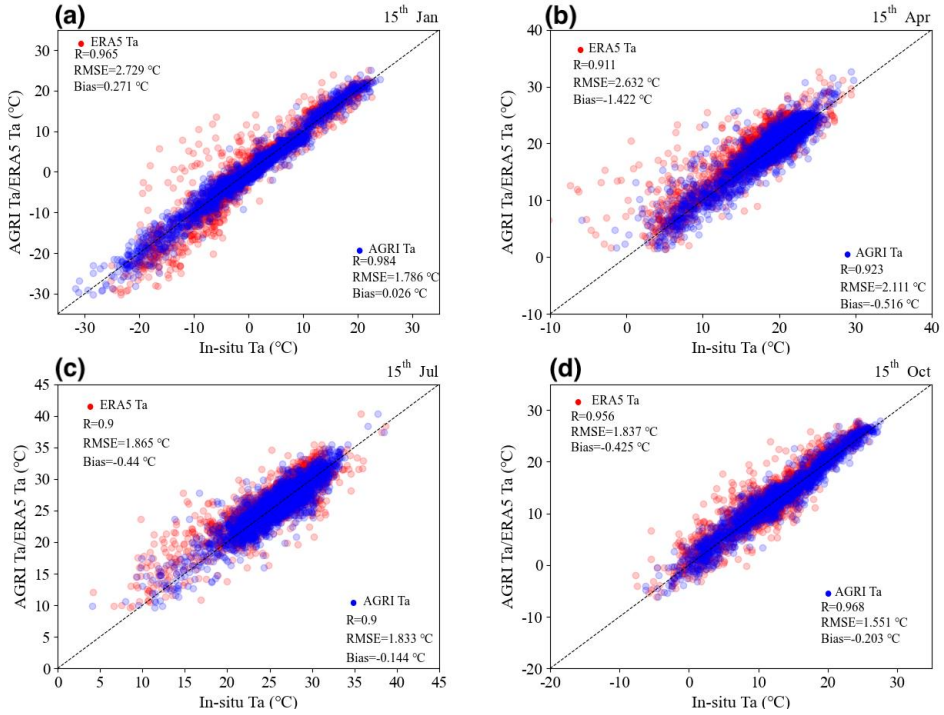

Figure 9. Comparisons of ERA5−Land and AGRI T_a with in situ T_a at 12:00 UTC, 15 January (**a**), April (**b**), July (**c**), and October (**d**) 2020.

The AGRI T_a accuracy at four times was better than that of the ERA5-Land, characterized by small RMSE and large R values. The RMSE of the AGRI T_a ranged from 1.55 to 2.11 °C, while that of the ERA5-Land ranged from 1.83 to 2.72 °C. It is worth noting that ERA5 showed an obvious negative bias when the T_a was less than −10 °C for 00 UTC on 15 January (i.e., DOY 15), suggesting that the T_a values over the Tibetan Plateau were underestimated. This also indicated that the AGRI-estimated T_a was more reliable than the ERA5-Land data. Additionally, the low spatial resolution of ERA5 and GFS may hinder their ability to accurately capture complex terrain and local temperature variations, resulting in larger temperature estimation errors.

In addition, AGRI T_a could show more details about T_a due to the higher spatial resolution, especially for complex terrain areas. As an example, Figure 10 shows a comparison of GFS-, ERA5-Land-, and AGRI-estimated all-weather T_a values over Sichuan province, China, at 12:00 UTC on 15 July 2020. Sichuan province, located in the southwest of China, has a complex and diverse terrain. From the west to the east of Sichuan, the terrain gradually decreases, with a huge terrain drop of nearly 7000 m. The western Sichuan region is dominated by plateau and mountain terrain, with an elevation of more than 3000 m. Eastern Sichuan is dominated by a basin (i.e., the Sichuan Basin) and hills, with an elevation of 500–2000 m.

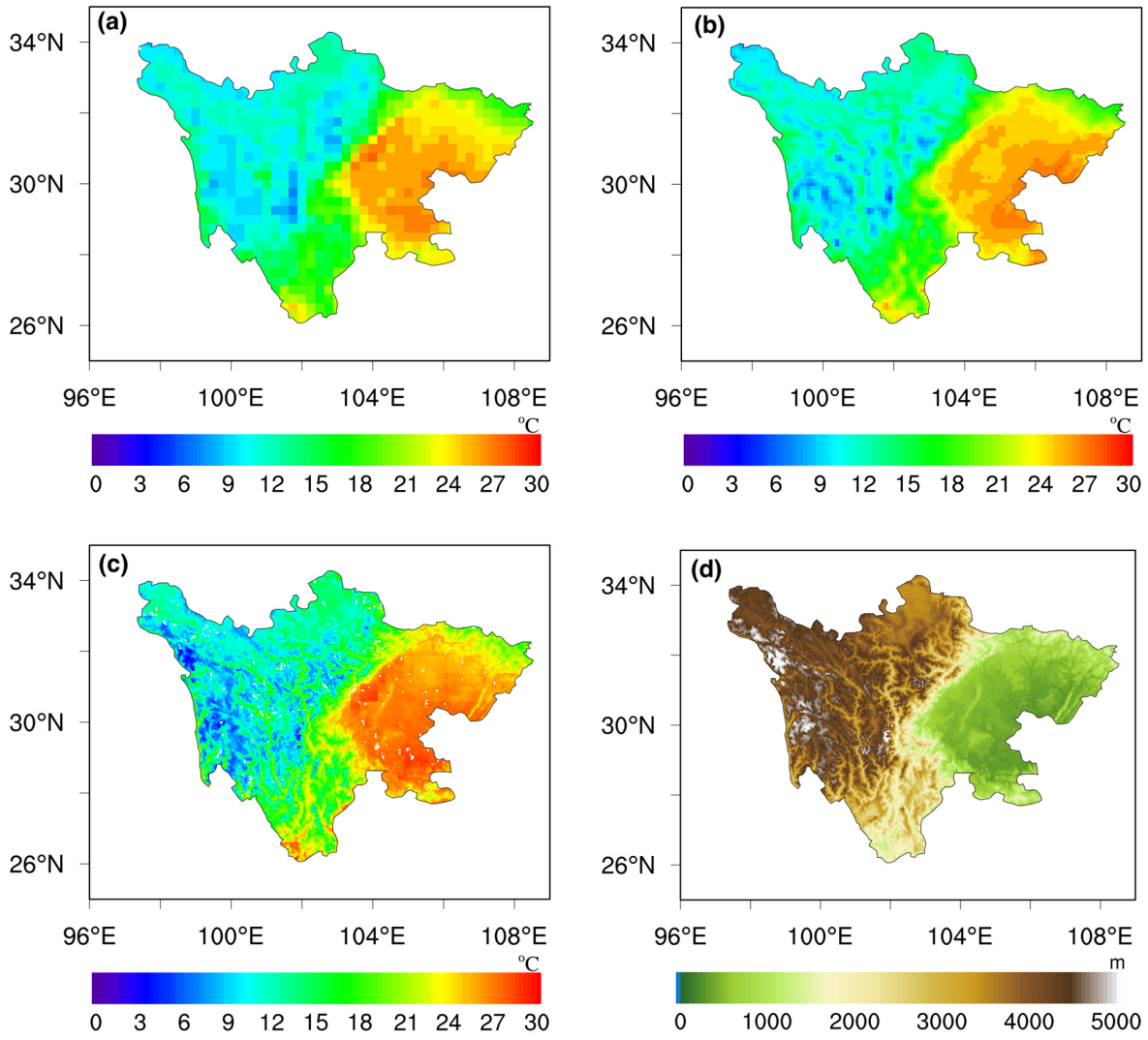

Figure 10. Comparison of the spatial pattern of all-weather T_a estimated by GFS (**a**), ERA5-Land (**b**), and AGRI (**c**) over Sichuan province at 12:00 UTC on 15 July 2020. The elevation distribution map of Sichuan Province (**d**) is also presented.

Influenced by topography, there were clear T_a differences between the eastern and western parts of Sichuan province. The T_a in the Sichuan Basin reached 30 °C at 00 UTC on 15 July 2020, while the T_a in the western plateau was lower than 0 °C. The AGRI model can better capture the spatial distribution details of air temperature (Figure 10), which gives it obvious advantages in T_a-related research and applications over complex-terrain areas. In addition, it can also provide finer data for studies of T_a diurnal variation characteristics and urban heat island effects.

3.5. Model Sensitivity Analysis

The contribution and sensitivity of each input to the $T_{a,clear}$ and $T_{a,cloudy}$ model were first analyzed using Simlab 2.2 software. Figure 11 shows the normalized total sensitivity index of each predictor for the $T_{a,clear}$ and $T_{a,cloud}$ estimation models.

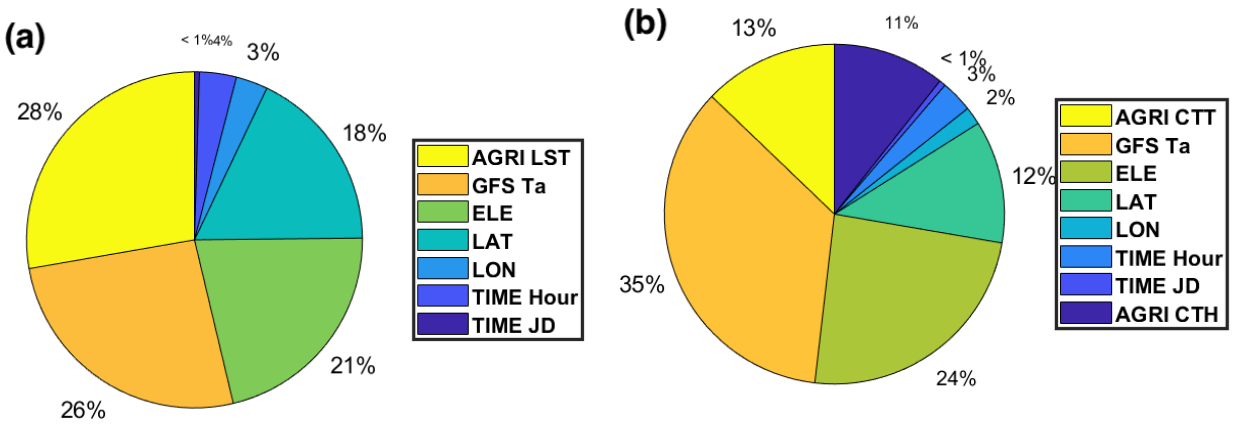

Figure 11. Normalized total sensitivity indexes for predictors of $T_{a,clear}$ (**a**) and $T_{a,cloud}$ (**b**) estimation models.

In general, the AGRI data, GFS T_a, elevation, and latitude had higher total sensitivity index than the other inputs. For clear sky, AGRI LST showed the largest total sensitivity index (~28%). The total sensitivity indexes for GFS T_a, elevation, and latitude were 26%, 21% and 18%. In contrast, the total sensitivity indexes of longitudes, JD, and hour were generally less than 4%. For cloudy sky, GFS T_a showed the highest total sensitivity index, with a value of 35%. The total sensitivity indexes of AGRI CTT and CTH were about 13% and 11%. The sensitivity indexes of elevation and latitude in the cloudy model were 24% and 12%, respectively. This indicates that AGRI, GFS, elevation, and latitude play an important role in T_a estimation in clear and cloudy conditions. Furthermore, the contribution of GFS in high-elevation areas (i.e., ELE > 1000 m) is less than that in low elevation areas (i.e., ELE < 1000 m). This is understandable because the GFS accuracy in high-altitude areas is lower than that in low-elevation areas. In contrast, the contributions of AGRI LST at different elevations are comparable.

It is worth mentioning that the errors in the latitude, longitude, JD, and hour in the model are usually negligible, so their contributions are relatively stable. In contrast, the total sensitivity index of the AGRI and GFS data is more closely related to their precision. If the accuracy of GFS T_a is higher than that of AGRI LST, we believe that the contribution of GFS will be larger than that of AGRI LST for T_a estimation. At present, the contribution of the AGRI is slightly larger than that of the GFS T_a in the clear-sky model. In comparison, the contribution of the GFS T_a is larger than that of the AGRI in the cloudy-sky model, which may be related to the higher accuracy of GFS T_a in cloudy sky. With the improvement in the accuracy of AGRI and GFS products, their contributions will also be improved. It is necessary to improve the accuracy of satellites and GFS to obtain higher-precision T_a.

Furthermore, the model sensitivity analysis was performed regarding elevation, T_a, LST, and CTT for different intervals. The elevation intervals were set to 0.2 km, while those of T_a, LST, and CTT were set to 5.0 °C. Figure 12 shows the dependence of RMSE and bias

on the elevation and T_a. The RMSE for both two models increased with elevation, while it decreased with T_a. The RMSE values were mainly <2.0 °C when the elevation was <2.0 km, while they reached up to 3.0 °C when the elevation was >4.0 km.

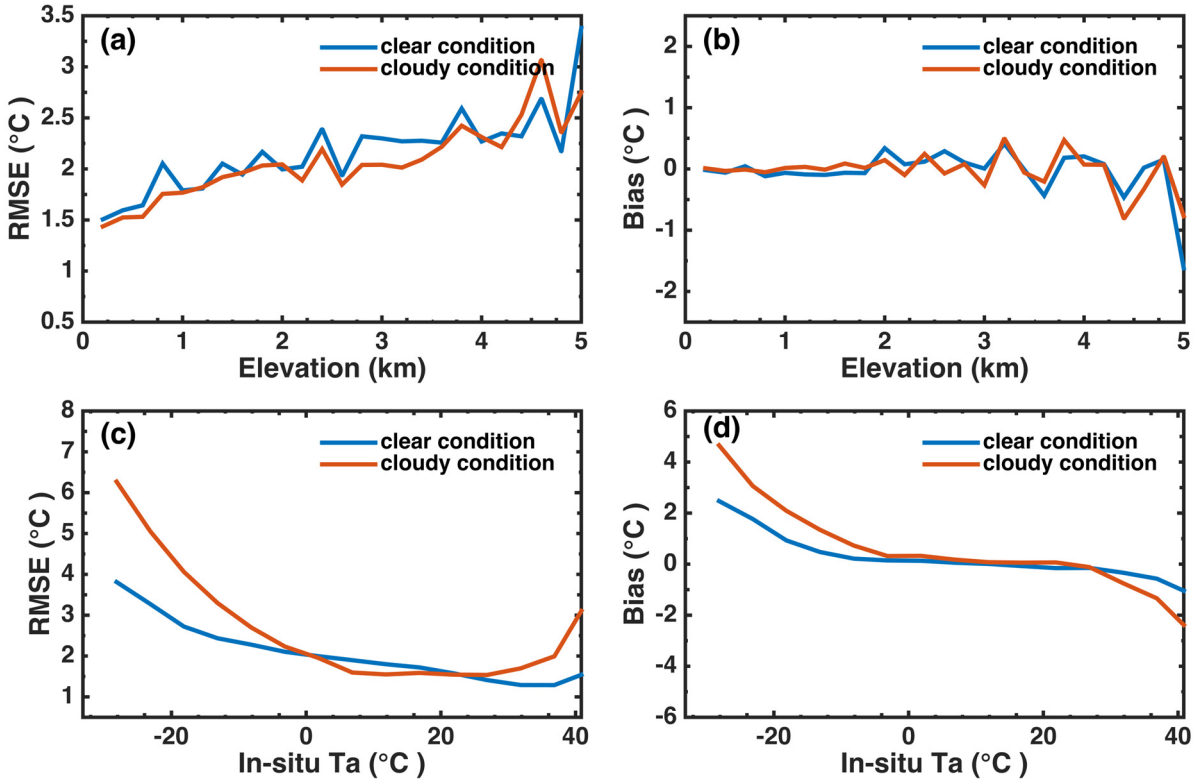

Figure 12. Dependence of the RMSE (**a**,**c**) and bias (**b**,**d**) of the AGRI T_a estimation models on elevation and T_a for clear and cloudy conditions.

The RMSE values for the clear and cloudy models were mainly <2.0 °C when $T_a > -5.0$ °C. The RMSE increased obviously with the decrease in T_a when $T_a < -5.0$ °C, and it reached up to 3.0 °C and 5.0 °C for clear and cloudy sky when the T_a was <−25 °C. The biases were within ±0.5 °C when the T_a ranged from −10.0 to 35.0 °C. However, the model showed obvious overestimation (i.e., bias >1.0 °C) when $T_a < -10.0$ °C.

Generally, the models produced a large error in low-T_a conditions (i.e., <−10 °C). This might have been due to the following reasons: (1) the low T_a mainly occurred in winter over western and northeastern China, which have fewer stations than other areas (Figure 1). Therefore, the applicability of the model to low-T_a conditions was worse due to the smaller number of training datasets. (2) The accuracy of the GFS T_a in winter was generally worse than in other seasons (Figure 6). As one of the key input factors of the model, this might result in relatively poor estimation accuracy under low-T_a conditions.

The RMSE values of the clear- and cloudy-sky models also showed a clear dependence on LST and CTT (Figure 13). The RMSE values of $T_{a,clear}$ and $T_{a,cloudy}$ decreased with LST and CTT, respectively. This indicated that the estimated T_a was more accurate at higher LST and CTT. The higher LST mainly occurred in summer, and the sensitivity analysis aligned with the seasonal characteristics of the model errors. High CTT mainly corresponded with warm low clouds, which indicated that the $T_{a,cloudy}$ estimation had better accuracy under warm low clouds. This was also consistent with the seasonal variation of the $T_{a,cloudy}$ error characteristics and previous studies [36].

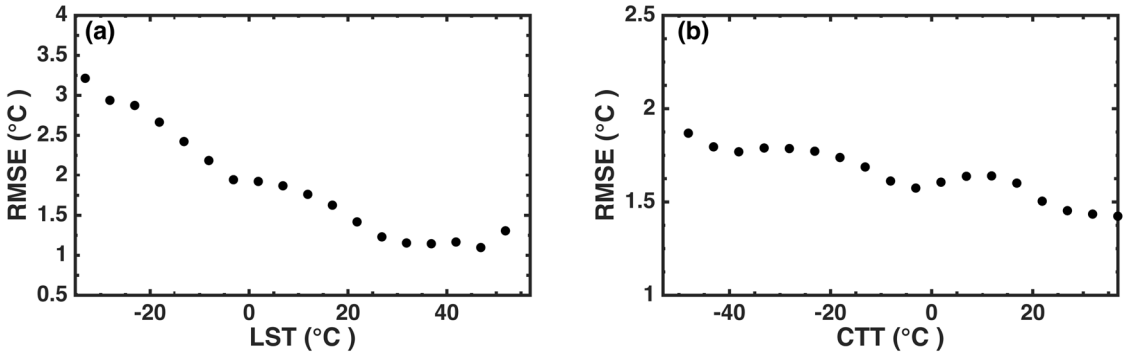

Figure 13. Dependence of the RMSE on LST and CTT for $T_{a,clear}$ (**a**) and $T_{a,cloudy}$ (**b**) models.

4. Discussion

The proposed temperature estimation model offers significant advancements over previous approaches. By incorporating all-weather conditions, it extends beyond clear-sky models to estimate temperatures under both clear and cloudy conditions using separate neural networks for each scenario. Additionally, the integration of GFS temperature forecast data enhances the model's accuracy across diverse weather situations. The model's reliability is further supported by its training and validation on independent datasets from 2423 stations, ensuring robust performance evaluation. These improvements make the model more versatile and reliable for temperature estimation under varying atmospheric conditions.

Additionally, the model exhibits temperature estimation errors during winter and in high-altitude regions. This may be attributed to the larger temperature fluctuations in winter and the model's suboptimal performance under extremely low temperatures. In high-altitude areas, complex terrain and elevation differences complicate temperature variation, and uncertainties in the environmental lapse rate further increase the difficulty of accurate estimation. Moreover, GFS data errors in these regions are higher compared to lower altitudes, contributing to the inaccuracies in temperature estimation. Future research will focus on improving the model by incorporating additional data to enhance temperature estimation accuracy in these areas.

Although the model proposed in this study has improved T_a estimation accuracy and data availability, there are still some uncertainties, and further research is needed to improve the results. Uncertainties in AGRI products may propagate through T_a estimation models. As AGRI LST, CTT, and CTH are critical inputs, their precision significantly affects model outcomes. However, the lack of dependable data makes it challenging to evaluate the accuracy of LST, CTT, and CTH. The errors' effects on the T_a estimation model require further investigation. The distribution of the stations used for the model's construction was uneven. Introducing more regional weather stations could enhance accuracy, particularly in western China. Since there are no LST, CTT, and CTH data available in the AGRI's probable clear-sky and probable cloudy-sky pixels, the T_a at these pixels is not estimated. The pixels can be filled with GFS in practical applications. The proposed algorithm can also be adapted for other geostationary satellites, like Himawari-8/9 and GOES-16/17.

For regions with complex terrain, such as the Tibetan Plateau and Sichuan Basin, further optimization of the model is needed to improve temperature estimation accuracy. Future research will focus on incorporating additional meteorological station data from these areas, adding terrain features like slope and surface roughness. These measures are expected to enhance the model's performance in high-altitude and complex-terrain regions and improve its adaptability to varying climate conditions.

5. Conclusions

An all-weather T_a estimation method was proposed using the AGRI and GFS products and additional parameters. The RMSE of the estimated T_a was less than 1.8 °C, demonstrat-

ing superior accuracy compared to the ERA5-Land data. This indicated that all-weather T_a can be estimated using AGRI and auxiliary data. This proposed model can be applied to other geostationary satellites. This study offers a new insight into the all-weather T_a estimation from satellite observations.

The neural-network-based model was established and validated using the data from 2423 stations in China during 2020. The T_a estimation model errors exhibited clear spatiotemporal variation characteristics, with higher accuracy during summer and poor accuracy during winter. The performance of the model in southeastern China was substantially better than that in western China. This might be related to topography, station density, the dynamic range of T_a changes, and GFS error characteristics. The accuracy of the AGRI-estimated T_a was surpassed that of the ERA5-Land, particularly for areas with high elevation. This also showed the good potential and robustness of the proposed models for all-weather T_a estimation. A global sensitivity analysis of the inputs for the T_a estimation model was performed. AGRI and GFS data are the most important factors for accurate T_a estimation. It is necessary to improve the accuracy of satellites and GFS to obtain higher-precision T_a.

Author Contributions: Conceptualization, H.-L.L. and M.-Z.D.; methodology, H.-L.L.; software, H.-L.L.; validation, H.-L.L. and M.-Z.D.; formal analysis, H.-L.L.; investigation, X.-Q.Z.; resources, M.-Z.D.; data curation, X.-Q.Z.; writing—original draft preparation, H.-L.L.; writing—review and editing, H.-L.L. and M.-Z.D.; visualization, X.-B.D. and M.-L.Z.; supervision, S.-L.Z.; project administration, H.-L.L.; funding acquisition, H.-L.L. and M.-Z.D. All authors have read and agreed to the published version of the manuscript.

Funding: This study is supported by the National Natural Science Foundation of China, grant number 42030107 and 42175150.

Data Availability Statement: The station data were downloaded through the China Meteorological Data Service Centre (CMDC) at https://data.cma.cn/en/ (accessed on 12 August 2024). The FY-4A data were obtained through FENGYUN Satellite Data Center of the National Satellite Meteorological Center at http://satellite.nsmc.org.cn/PortalSite/Data/Satellite.aspx (accessed on 12 August 2024). The GFS historical data were downloaded from the National Center for Atmospheric Research (NCAR) at https://rda.ucar.edu (accessed on 12 August 2024). The ERA5-Land hourly 2 m T_a ($T_{a,\,ERA5}$) in 2020 were obtained at the Copernicus Climate Data Store at https://cds.climate.copernicus.eu/(accessed on 12 August 2024). The SRTM3 data are from the USGS Earth Explorer at https://earthexplorer.usgs.gov (accessed on 12 August 2024).

Acknowledgments: This work was supported by the National Natural Science Foundation of China, grant numbers 42030107 and 42175150. The authors would like to thank NSMC, CMDC, and NCAR for providing AGRI, meteorological, and GFS data. We also thank ECMWF and NASA for providing ERA5-Land, MODIS NDVI, and SRTM3 data.

Conflicts of Interest: The authors declare no conflicts of interest.

References

1. Prince, S.D.; Goward, S.N. Global Primary Production: A Remote Sensing Approach. *J. Biogeogr.* **1995**, *22*, 815–835. [CrossRef]
2. Yang, Y.Z.; Cai, W.H.; Yang, J. Evaluation of MODIS Land Surface Temperature Data to Estimate Near-Surface Air Temperature in Northeast China. *Remote Sens.* **2017**, *9*, 410. [CrossRef]
3. Santer, B.D.; Wigley, T.M.L.; Mears, C.; Wentz, F.J.; Klein, S.A.; Seidel, D.J.; Taylor, K.E.; Thorne, P.W.; Wehner, M.F.; Gleckler, P.J.; et al. Amplification of surface temperature trends and variability in the tropical atmosphere. *Science* **2005**, *309*, 1551–1556. [CrossRef] [PubMed]
4. Lin, S.P.; Moore, N.J.; Messina, J.P.; DeVisser, M.H.; Wu, J.P. Evaluation of estimating daily maximum and minimum air temperature with MODIS data in east Africa. *Int. J. Appl. Earth Obs. Geoinf.* **2012**, *18*, 128–140. [CrossRef]
5. Good, E.J. An in situ-based analysis of the relationship between land surface "skin" and screen-level air temperatures. *J. Geophys. Res. Atmos.* **2016**, *121*, 8801–8819. [CrossRef]
6. Błażejczyk, K.; Jendritzky, G.; Bröde, P.; Fiala, D.; Havenith, G.; Epstein, Y.; Psikuta, A.; Kampmann, B. An introduction to the universal thermal climate index (UTCI). *Geogr. Pol.* **2013**, *86*, 5–10. [CrossRef]

7. Woolway, R.I.; Sharma, S.; Weyhenmeyer, G.A.; Debolskiy, A.; Golub, M.; Mercado-Bettín, D.; Perroud, M.; Stepanenko, V.; Tan, Z.L.; Grant, L.; et al. Phenological shifts in lake stratification under climate change. *Nat. Commun.* **2021**, *12*, 11. [CrossRef] [PubMed]
8. He, J.; Yang, K.; Tang, W.J.; Lu, H.; Qin, J.; Chen, Y.Y.; Li, X. The first high-resolution meteorological forcing dataset for land process studies over China. *Sci. Data* **2020**, *7*, 11. [CrossRef]
9. Prihodko, L.; Goward, S.N. Estimation of air temperature from remotely sensed surface observations. *Remote Sens. Environ.* **1997**, *60*, 335–346. [CrossRef]
10. Gholamnia, M.; Alavipanah, S.K.; Darvishi Boloorani, A.; Hamzeh, S.; Kiavarz, M. Diurnal Air Temperature Modeling Based on the Land Surface Temperature. *Remote Sens.* **2017**, *9*, 915. [CrossRef]
11. Yao, R.; Wang, L.C.; Huang, X.; Li, L.; Sun, J.; Wu, X.J.; Jiang, W.X. Developing a temporally accurate air temperature dataset for Mainland China. *Sci. Total Environ.* **2020**, *706*, 12. [CrossRef] [PubMed]
12. Zhou, J.; Zhang, X.D.; Zhan, W.F.; Göttsche, F.M.; Liu, S.M.; Olesen, F.S.; Hu, W.X.; Dai, F.N. A Thermal Sampling Depth Correction Method for Land Surface Temperature Estimation From Satellite Passive Microwave Observation Over Barren Land. *IEEE Trans. Geosci. Remote Sens.* **2017**, *55*, 4743–4756. [CrossRef]
13. Ding, L.R.; Zhou, J.; Zhang, X.D.; Liu, S.M.; Cao, R.Y. Downscaling of surface air temperature over the Tibetan Plateau based on DEM. *Int. J. Appl. Earth Obs. Geoinf.* **2018**, *73*, 136–147. [CrossRef]
14. Rao, Y.H.; Liang, S.L.; Wang, D.D.; Yu, Y.Y.; Song, Z.; Zhou, Y.; Shen, M.G.; Xu, B.Q. Estimating daily average surface air temperature using satellite land surface temperature and top-of-atmosphere radiation products over the Tibetan Plateau. *Remote Sens. Environ.* **2019**, *234*, 14. [CrossRef]
15. Shen, H.F.; Jiang, Y.; Li, T.W.; Cheng, Q.; Zeng, C.; Zhang, L.P. Deep learning-based air temperature mapping by fusing remote sensing, station, simulation and socioeconomic data. *Remote Sens. Environ.* **2020**, *240*, 14. [CrossRef]
16. Vancutsem, C.; Ceccato, P.; Dinku, T.; Connor, S.J. Evaluation of MODIS land surface temperature data to estimate air temperature in different ecosystems over Africa. *Remote Sens. Environ.* **2010**, *114*, 449–465. [CrossRef]
17. Yao, R.; Wang, L.C.; Huang, X.; Cao, Q.; Peng, Y.Y. A method for improving the estimation of extreme air temperature by satellite. *Sci. Total Environ.* **2022**, *837*, 12. [CrossRef] [PubMed]
18. Zou, J.; Lu, N.; Jiang, H.; Qin, J.; Yao, L.; Xin, Y.; Su, F.Z. Performance of air temperature from ERAS-Land reanalysis in coastal urban agglomeration of Southeast China. *Sci. Total Environ.* **2022**, *828*, 13. [CrossRef] [PubMed]
19. Qin, J.; He, M.; Jiang, H.; Lu, N. Reconstruction of 60-year (1961–2020) surface air temperature on the Tibetan Plateau by fusing MODIS and ERA5 temperatures. *Sci. Total Environ.* **2022**, *853*, 13. [CrossRef]
20. An, S.; Zhu, X.L.; Shen, M.G.; Wang, Y.F.; Cao, R.Y.; Chen, X.H.; Yang, W.; Chen, J.; Tang, Y.H. Mismatch in elevational shifts between satellite observed vegetation greenness and temperature isolines during 2000–2016 on the Tibetan Plateau. *Glob. Chang. Biol.* **2018**, *24*, 5411–5425. [CrossRef] [PubMed]
21. Liu, H.L.; Zhou, Q.; Zhang, S.L.; Deng, X.B. Estimation of Summer Air Temperature over China Using Himawari-8 AHI and Numerical Weather Prediction Data. *Adv. Meteorol.* **2019**, *2019*, 10. [CrossRef]
22. Good, E. Daily minimum and maximum surface air temperatures from geostationary satellite data. *J. Geophys. Res. Atmos.* **2015**, *120*, 2306–2324. [CrossRef]
23. Zaksek, K.; Schroedter-Homscheidt, M. Parameterization of air temperature in high temporal and spatial resolution from a combination of the SEVIRI and MODIS instruments. *ISPRS-J. Photogramm. Remote Sens.* **2009**, *64*, 414–421. [CrossRef]
24. Cresswell, M.P.; Morse, A.P.; Thomson, M.C.; Connor, S.J. Estimating surface air temperatures, from Meteosat land surface temperatures, using an empirical solar zenith angle model. *Int. J. Remote Sens.* **1999**, *20*, 1125–1132. [CrossRef]
25. Karimi, S.M.; Kisi, O.; Porrajabali, M.; Rouhani-Nia, F.; Shiri, J. Evaluation of the support vector machine, random forest and geo-statistical methodologies for predicting long-term air temperature. *ISH J. Hydraul. Eng.* **2018**, *26*, 376–386. [CrossRef]
26. Mao, K.B.; Tang, H.J.; Wang, X.F.; Zhou, Q.B.; Wang, D.L. Near-surface air temperature estimation from ASTER data based on neural network algorithm. *Int. J. Remote Sens.* **2008**, *29*, 6021–6028. [CrossRef]
27. Zhu, X.D.; Zhang, Q.; Xu, C.Y.; Sun, P.; Hu, P. Reconstruction of high spatial resolution surface air temperature data across China: A new geo-intelligent multisource data-based machine learning technique. *Sci. Total Environ.* **2019**, *665*, 300–313. [CrossRef] [PubMed]
28. Czajkowski, K.P.; Goward, S.N.; Stadler, S.J.; Walz, A. Thermal Remote Sensing of Near Surface Environmental Variables: Application Over the Oklahoma Mesonet. *Prof. Geogr.* **2010**, *52*, 345–357. [CrossRef]
29. Zhu, W.B.; Lü, A.F.; Jia, S.F. Estimation of daily maximum and minimum air temperature using MODIS land surface temperature products. *Remote Sens. Environ.* **2013**, *130*, 62–73. [CrossRef]
30. Sun, Y.J.; Wang, J.F.; Zhang, R.H.; Gillies, R.R.; Xue, Y.; Bo, Y.C. Air temperature retrieval from remote sensing data based on thermodynamics. *Theor. Appl. Climatol.* **2005**, *80*, 37–48. [CrossRef]
31. Zhang, R.H.; Rong, Y.; Tian, J.; Su, H.B.; Li, Z.L.; Liu, S.H. A Remote Sensing Method for Estimating Surface Air Temperature and Surface Vapor Pressure on a Regional Scale. *Remote Sens.* **2015**, *7*, 6005–6025. [CrossRef]
32. Zhang, Z.; Liang, Y.; Zhang, G.; Liang, C. Large-Scale Estimation of Hourly Surface Air Temperature Based on Observations from the FY-4A Geostationary Satellite. *Remote Sens.* **2023**, *15*, 1753. [CrossRef]
33. Jang, K.; Kang, S.; Kimball, J.S.; Hong, S.Y. Retrievals of All-Weather Daily Air Temperature Using MODIS and AMSR-E Data. *Remote Sens.* **2014**, *6*, 8387–8404. [CrossRef]

34. Meraner, A.; Ebel, P.; Zhu, X.X.; Schmitt, M. Cloud removal in Sentinel-2 imagery using a deep residual neural network and SAR-optical data fusion. *ISPRS-J. Photogramm. Remote Sens.* **2020**, *166*, 333–346. [CrossRef] [PubMed]
35. Liu, H.; Chen, Y.; Han, Q.; Deng, X.; Fan, J.; Duan, M.; Huang, Q. Estimation of high spatial resolution all-weather near-surface air temperature using FY-4A AGRI observations. *Atmos. Res.* **2023**, *285*, 106642. [CrossRef]
36. Li, H.P.; Liu, H.L.; Duan, M.Z.; Deng, X.B.; Zhang, S.L. Estimation of Air Temperature under Cloudy Conditions Using Satellite-Based Cloud Products. *IEEE Geosci. Remote Sens. Lett.* **2022**, *19*, 5. [CrossRef]
37. Liu, S.H.; Su, H.B.; Tian, J.; Zhang, R.H.; Wang, W.Z.; Wu, Y.R. Evaluating Four Remote Sensing Methods for Estimating Surface Air Temperature on a Regional Scale. *J. Appl. Meteorol. Climatol.* **2017**, *56*, 803–814. [CrossRef]
38. Wagner, W.; Naeimi, V.; Scipal, K.; de Jeu, R.; Martínez-Fernández, J. Soil moisture from operational meteorological satellites. *Hydrogeol. J.* **2007**, *15*, 121–131. [CrossRef]
39. Zhihua, R.; Anyuan, X. Operational System Development on Three-step Quality Control of Observations from AWS. *Meteorol. Mon.* **2007**, *33*, 19–24.
40. Zhang, P.; Zhu, L.; Tang, S.H.; Gao, L.; Chen, L.; Zheng, W.; Han, X.Z.; Chen, J.; Shao, J.L. General Comparison of FY-4A/AGRI with Other GEO/LEO Instruments and Its Potential and Challenges in Non-meteorological Applications. *Front. Earth Sci.* **2019**, *6*, 13. [CrossRef]
41. Dong, L.; Xu, N.; Chen, L. Retrieval of FY-4A Land Surface Temperature for Operational Application. In Proceedings of the EGU General Assembly Conference Abstracts, Online, 4–8 May 2020.
42. Ulivieri, C.; Cannizzaro, G. Land surface temperature retrievals from satellite measurements. *Acta Astronaut.* **1985**, *12*, 977–985. [CrossRef]
43. Tan, Z.H.; Ma, S.; Zhao, X.B.; Yan, W.; Lu, W. Evaluation of Cloud Top Height Retrievals from China's Next-Generation Geostationary Meteorological Satellite FY-4A. *J. Meteorol. Res.* **2019**, *33*, 553–562. [CrossRef]
44. Liu, B.; Huo, J.; Lyu, D.R.; Wang, X. Assessment of FY-4A and Himawari-8 Cloud Top Height Retrieval through Comparison with Ground-Based Millimeter Radar at Sites in Tibet and Beijing. *Adv. Atmos. Sci.* **2021**, *38*, 1334–1350. [CrossRef]
45. Cao, B.; Gruber, S.; Zheng, D.; Li, X. The ERA5-Land soil temperature bias in permafrost regions. *Cryosphere* **2020**, *14*, 2581–2595. [CrossRef]
46. Zhou, K.; Liu, H.L.; Deng, X.B.; Wang, H.; Zhang, S.L. Comparison of Machine-Learning Algorithms for Near-Surface Air-Temperature Estimation from FY-4A AGRI Data. *Adv. Meteorol.* **2020**, *2020*, 14. [CrossRef]
47. Zhu, W.B.; Lu, A.F.; Jia, S.F.; Yan, J.B.; Mahmood, R. Retrievals of all-weather daytime air temperature from MODIS products. *Remote Sens. Environ.* **2017**, *189*, 152–163. [CrossRef]
48. Du, M.X.; Zhang, M.J.; Wang, S.J.; Zhu, X.F.; Che, Y.J. Near-surface air temperature lapse rates in Xinjiang, northwestern China. *Theor. Appl. Climatol.* **2018**, *131*, 1221–1234. [CrossRef]
49. Li, X.P.; Wang, L.; Chen, D.L.; Yang, K.; Xue, B.L.; Sun, L.T. Near-surface air temperature lapse rates in the mainland China during 1962–2011. *J. Geophys. Res. Atmos.* **2013**, *118*, 7505–7515. [CrossRef]
50. Wang, Y.; Wang, L.; Li, X.; Chen, D. Temporal and spatial changes in estimated near-surface air temperature lapse rates on Tibetan Plateau. *Int. J. Climatol.* **2018**, *38*, 2907–2921. [CrossRef]
51. Benali, A.; Carvalho, A.C.; Nunes, J.P.; Carvalhais, N.; Santos, A. Estimating air surface temperature in Portugal using MODIS LST data. *Remote Sens. Environ.* **2012**, *124*, 108–121. [CrossRef]
52. Shi, Y.; Jiang, Z.H.; Dong, L.P.; Shen, S.H. Statistical estimation of high-resolution surface air temperature from MODIS over the Yangtze River Delta, China. *J. Meteorol. Res.* **2017**, *31*, 448–454. [CrossRef]
53. Li, X.M.; Zhou, Y.Y.; Asrar, G.R.; Zhu, Z.Y. Developing a 1 km resolution daily air temperature dataset for urban and surrounding areas in the conterminous United States. *Remote Sens. Environ.* **2018**, *215*, 74–84. [CrossRef]
54. Oyler, J.W.; Ballantyne, A.; Jencso, K.; Sweet, M.; Running, S.W. Creating a topoclimatic daily air temperature dataset for the conterminous United States using homogenized station data and remotely sensed land skin temperature. *Int. J. Climatol.* **2015**, *35*, 2258–2279. [CrossRef]